PAPER

CrossMark
click for updates

Large-area high-efficiency perovskite solar cells based on perovskite films dried by the multi-flow air knife method in air†

Li-Li Gao, Cheng-Xin Li, Chang-Jiu Li and Guan-Jun Yang*

Perovskite solar cells are extremely promising high-efficiency low-cost photovoltaic devices. However, large-area and uniform perovskite film fabrication in air is still a big challenge for the mass production of highly efficient perovskite solar cells. Here, we first report the novel multi-flow air knife (MAK) method to control the formation of large-area perovskite films in ambient air. The proposed MAK method, based on the comprehensive understanding of the solution film evaporation process, entails the use of multiple gas flows that rapidly dry the solution and enable the production of large-area perovskite films in air. By adopting the MAK technology, high-quality films with full surface coverage and a low surface roughness of 4.98 nm over a $10 \times 10 \ \mu m^2$ scan area were successfully fabricated. Highly reproducible power conversion efficiencies up to 11.70% were achieved with an active area of 1.0 cm^2. The highest efficiency of 17.71%, obtained for a device with an area of 0.1 cm^2, further demonstrated the promising potential of this technology. Thus, the MAK technology enables the low-cost fabrication of highly efficient perovskite solar cells, paving the way for the mass production of low-cost high-performance perovskite solar cells in ambient air.

Introduction

Metal-halide perovskite solar cells have attracted enormous interest and extensive research due to the excellent achievements in the field of third generation photovoltaic devices, which focus on providing clean energy for humans in the future. Their power conversion efficiencies have skyrocketed from 3.8% (ref. 1) to values higher than 20% (ref. 2–4) in just about 5 years. Metal-halide perovskite is an outstanding photoabsorber and carrier transporter, owing to its high extinction coefficient, excellent ambipolar charge mobility, small exciton binding energy, and tunable bandgap.[4–7] Perovskite solar cells can be easily and cheaply prepared by using solution processing methods through high-yield printing and coating technologies, which are attractive for low-cost large-area solar energy harvesting in industrial applications.

For scaling-up and commercialization of perovskite-based devices, the continuous fabrication of pinhole-free perovskite films in air is crucial. However, to date, this is a great challenge due to the lack of a clear understanding of the precipitation process of solid perovskite from a solution. Notably, a good delivery efficiency in perovskite solar cells essentially depends on a compact pin-hole free perovskite film, which can lead to excellent electrical performances.[8] As a crucial layer, the perovskite film is widely prepared by solution processing methods, and great achievements have led to highly efficient solar cells.[8–13] The active device area has also increased from 0.035,[14] 0.04,[15] and 0.09 cm^2,[16] to 1 cm^2,[17,18] which is a groundbreaking value and accelerates industrial application. However, large-area perovskite film fabrication in air is still a great challenge. High-cost vacuum technology can hardly produce high-quality perovskite films over large areas,[19,20] and thus, for perovskite solar cell industrialization, large-area films prepared in ambient air are necessary.

To fabricate high-quality perovskite films, various thin-film deposition technologies including spray deposition,[21] spin coating,[12,22] doctor blading,[23,24] printing,[25,26] and slot-die coating[27] have been adopted. In our previous study, we proposed a gas pump method to produce full-coverage perovskite films, reporting 19% efficiency for devices on rigid glass and 11.34% efficiency for devices on a plastic substrate.[28–30] Recently, a certified efficiency of 19.6% for devices fabricated by using this method (named as vacuum flash-assisted solution process) was reported.[31] Although highly compact perovskite films cannot be fabricated by using only solution deposition technologies, the film drying process enables the critical formation of a solid pin-hole free film upon precipitation of solid perovskite from a supersaturated solution. However, our current understanding of the phenomena occurring during the

State Key Laboratory for Mechanical Behavior of Materials, School of Materials Science and Engineering, Xi'an Jiaotong University, Xi'an, Shaanxi 710049, PR China. E-mail: ygj@mail.xjtu.edu.cn

drying process of a large-area solution film is considerably limited.

In this paper, we report for the first time the multi-flow air knife (MAK) method, which can be used to prepare large-area high-performance perovskite films at room temperature in ambient air. We also report a record efficiency of 11.70% for large-area perovskite solar cells (with an active area of 1 cm^2) fabricated by using the MAK method in ambient air. We successfully fabricated a full-coverage perovskite film with a surface roughness of 4.98 nm on a 10 × 10 μm^2 scan area, as measured *via* atomic force microscopy (AFM). The grains appeared uniform and close packed in the whole film. Planar perovskite solar cells were also fabricated with perovskite films, prepared by the MAK method, on 2.5 × 2.5 cm^2 substrates, and efficiencies as high as 11.70% and 17.71% were obtained for active areas of 1 and 0.1 cm^2, respectively. The devices showed good reproducibility due to excellent film quality. Device efficiencies of 10.20% ± 0.81% and 14.42% ± 1.34% were averaged over 40 solar cells with active areas of 1 cm^2 and 0.1 cm^2, respectively. We believe that the MAK method would promote the low-cost fabrication of highly efficient perovskite solar cells, paving the way for mass production of low-cost high-performance perovskite solar cells in ambient air.

Experimental section

Materials and preparation

Lead iodide (PbI$_2$, 99.99%), N,N-dimethylformamide (DMF, 99.8%), iodine methylamine (CH$_3$NH$_3$I), and 2,20,7,70-tetrakis(N,N-di-p-methoxyphenylamine)-9,9-spirobifluorene (spiro-OMeTAD) were purchased from Xi'an Polymer Light Technology Corp. Titanium dioxide precursor solvent was synthesized following the reported procedure.[32] All materials were used as received. The multi-flow air knife equipment was designed by our group.

Perovskite film fabrication

PbI$_2$ and CH$_3$NH$_3$I at a molar ratio of 1 : 1 were dissolved in DMF solvent. The perovskite precursor solution was stirred at 70 °C for 12 h and stored in a glovebox. An appropriate amount of perovskite precursor solution was dropped on the TiO$_2$-coated FTO surface and spun at 5000 rpm for 6 s; a faint yellow liquid perovskite precursor film of ∼2 μm in thickness was obtained. Subsequently, the MAK was quickly swept across the solution film at the fastest air flow rate. In this paper, we adopted the flow rate values of 150, 225, and 300 L min^{-1}, using some different comparative distances between the MAK and the solution film surface (0.5, 1, 2, 3, 4, and 5 mm). The dried films were annealed for 10 min at 100 °C on a hot plate.

Perovskite solar cell fabrication

Devices were fabricated on FTO-coated glass (Pilkington, 15 Ω sq^{-1}). The FTO substrates were rinsed successively with acetone, ethyl alcohol, and deionized water in an ultrasonic bath for 10 min, and then blow dried with nitrogen. The FTO substrates were treated with ozone and ultraviolet light for

15 min. An electron transport layer of compact TiO$_2$ was deposited by spin coating a mildly acidic solution of titanium isopropoxide in ethanol at 3000 rpm for 30 s, and sintered at 500 °C for 30 min. The hole-blocking layer of the compact TiO$_2$ layer was ∼50 nm thick. A dense perovskite film was prepared by the MAK method, ∼300 nm in thickness, on the TiO$_2$ layer. All the above steps were conducted under ambient conditions at a temperature of 20 ± 3 °C and humidity of 40 ± 5%. A spiro-OMeTAD solution (25 μL) was spin coated on perovskite films at 3000 rpm for 30 s. Devices were then left overnight in air to allow for the spiro-OMeTAD doping *via* oxidation. Finally, an 80 nm-thick Au layer was deposited by thermal evaporation under a vacuum of 4 × 10^{-4} Pa. The finished devices were stored in a N$_2$-purged glovebox (<0.1 ppm O$_2$ and H$_2$O) before measurement.

Measurement and characterization

The surface morphologies of the perovskite films were examined using SEM (VEGA II-XMU, TESCAN, Czech Republic). To analyze the roughness of the perovskite films, AFM (Bruker, Germany) was used to examine the surface profile. The XRD patterns of the FTO substrate, PbI$_2$, CH$_3$NH$_3$I, and perovskite films were obtained with a D8 Advance X-ray diffractometer with Cu K$_\alpha$ radiation. All samples were scanned from 10° to 60° with a step size of 0.2°. The absorption and photoluminescence spectra of the perovskite films were measured with a U-3010 spectrophotometer. I–V curves of the perovskite solar cells were measured by using a Keithley 2400 source-measure unit under the illumination of simulated sunlight, provided by a 450 W Class AAA solar simulator equipped with a filtered Xe lamp, (AM 1.5 G, 100 mW cm^{-2}, Sol3A, Oriel Instruments). The output light intensity was calibrated using a single-crystal silicon photovoltaic cell as the reference (91150V, Oriel Instruments). The cells were measured with a non-reflective metal mask covering areas of 0.1 and 1 cm^2 to receive sunlight and avoid light scattering through the edges. The current densities of the devices were measured by biasing the devices at the maximum power point for 150 s, and then calculating the steady-state power conversion efficiency. IPCE spectra of the devices were recorded in air without bias light by using a Qtest Station 1000ADX system (Growntech, Inc.). The illumination spot size was slightly smaller than the active area of the test cells. IPCE photocurrents were recorded under short-circuit conditions using a Keithley 2400 source meter. The monochromatic photon flux was quantified by means of a calibrated silicon photodiode. EIS analysis was conducted on a Zahner Ennium Electrochemical Workstation in the frequency range between 4 MHz and 100 mHz under illumination of 37 W m^2 at forward bias ranging from 0.0 to 1.0 V.

Results and discussion

Fabrication of large-area perovskite films by the MAK method

The general application of the MAK method to produce full-coverage large-area perovskite films is shown in Fig. 1a. First, a perovskite precursor solution is coated, for example by slot-die

This journal is © The Royal Society of Chemistry 2017

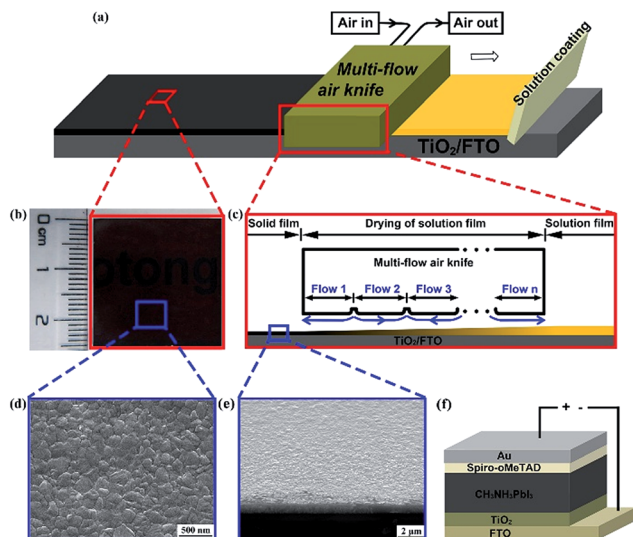*J. Mater. Chem. A*, 2017, **5**, 1548–1557 | **1549**

Fig. 1 (a) Schematic illustration of the perovskite solution film drying process by the multi-flow air knife (MAK) method. (b) Photograph of a single piece of perovskite film prepared by the MAK method. (c) Cross-sectional schematic diagram of the MAK setup. (d) Scanning electron microscopy (SEM) surface image of the perovskite film prepared by the MAK method. (e) Cross-sectional SEM image. (f) Structural diagram of the planar perovskite solar cell.
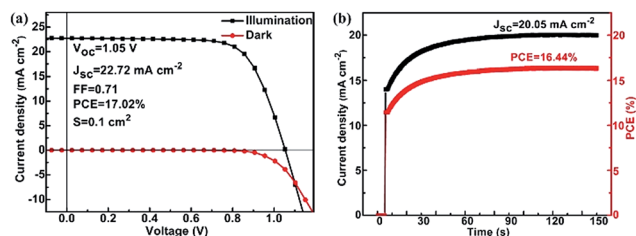

Fig. 2 Photovoltaic performance of the multi-flow air knife processed polymer solar cell. (a) Current–voltage curve for a device with an active area of 0.1 cm^2. (b) Corresponding steady-state current density and power conversion efficiency at a bias voltage of 0.82 V (the device was placed in the dark before the start of the steady-state measurement).

or doctor-blading technology (or spin coating in a lab), on a TiO$_2$-coated substrate to form a solution film with a light yellow color. Second, the solvent in the film is dried by sweeping the MAK from one side of the substrate to the other. Finally, the dried perovskite film is heated for 10 min. The dried perovskite film prepared by using the MAK method presented a mirror-like morphology with a black brown color. The large block substrate can then be cut into small pieces of 2.5 × 2.5 cm^2 (Fig. 1b), which are subsequently used to fabricate perovskite solar cells. The film, further analyzed by scanning electron microscopy (SEM, Fig. 1d), clearly appeared compact and free of pin holes over the whole area. The grain size distribution was quite uniform. The statistical results revealed that the grains had a size of ∼262 nm. As seen in the SEM image, flat polygonal grains with triple junction grain boundaries were the predominant microstructural feature, which suggested close packing of perovskite grains over the whole area.

Fig. 1c shows the cross-sectional schematic diagram of the MAK setup. When the MAK moves quickly on the liquid surface, multiple air flows from different channels sweep across the solution film surface with a certain speed, removing the solvent molecules away through air out. After the MAK sweeps over the whole solution film, a solid perovskite film is precipitated. The cross-sectional image showed a compact film made of closely packed columnar crystals (Fig. 1e). The MAK setup is flexible, and it allows sufficient air blowing over a short distance to dry the solution film. Moreover, the solution film size has no limitations, for example, a meter scale system for industrialization would be quite easy to realize.

To demonstrate the high performance of the produced perovskite film, planar perovskite solar cells were fabricated

with the structure shown in Fig. 1f, obtaining a 17.02% efficiency with an active area of 0.1 cm^2 (Fig. 2a). The open-circuit voltage (V_{oc}) was 1.05 V, short-circuit current (J_{sc}) was 22.72 mA cm^{-2}, and fill factor (FF) was 0.71. To determine a more realistic efficiency of the device by considering the hysteresis effect, a steady-state photocurrent was measured as a function of time at the forward bias of 0.82 V, which corresponds to the maximum power output according to the current–voltage (I–V) measurement (Fig. 2b). Under 1 sun continuous illumination, the steady-state photocurrent density stabilized at 20.05 mA cm^{-2}, and the power conversion efficiency (PCE) stabilized at 16.44% over 150 s, which was slightly lower (3%) than the PCE obtained from the I–V measurement.

Air-assisted flow has been previously used to dry liquid perovskite films,[10,27,33–35] although it can't be suitable for drying large-area solution films in ambient air. The solution films with areas of 5 × 5 cm^2 dried by air flow[27] showed inhomogeneous morphologies, turning from shiny to blurry, and some wave traces can be observed in macroscopic pictures. This corresponds to the transition from uniform isometric to thick dendritic crystals observed in microscopic pictures (Fig. S1a†). The change is attributed to the fact that the solubility of the air flow rapidly reaches saturation when the flow sweeps across a solution film at a very short distance along the flowing direction (parallel to the surface in this case), and the flow gives rise to waves on the liquid film surface. The saturated flow, which contains evaporated solvent molecules, cannot dissolve more molecules. Essentially, the reported air assisted methods are based on axis asymmetry, and therefore can't be successful for scale enlargement. In addition, a large distance between blowing air and the solution film hinders the diffusion of solvent molecules. As a result, the solution film cannot be thoroughly dried in a short time, as shown in Fig. S1b.†

To solve this crucial problem, in this study, we developed the MAK technique, which involves blowing air vertically on the liquid surface. It avoids the formation of waves on the liquid film surface. In this method, the saturated air on the surface of the solution film is removed in a timely fashion through air out, while, at the same time, fresh air is constantly flowed in. Such a circulation process facilitates the quick removal of the solvent by fresh air. The solution film (area of 5 × 5 cm^2) dried by using the MAK method exhibited a mirror-like black brown morphology, as shown in the photograph in Fig. S2.† To develop compact large-

1550 | J. Mater. Chem. A, 2017, 5, 1548–1557

This journal is © The Royal Society of Chemistry 2017

area perovskite films by the MAK method, a deep analysis and understanding of the evaporation process is necessary.

Understanding the essence of solvent evaporation

To better understand the evaporation phenomenon in thin solution films, the prerequisites for solvent evaporation were thoroughly researched. In perovskite precursor solutions, N,N-dimethylformamide (DMF) is typically used as the organic solvent. The evaporation process of DMF in a closed space from the starting state (consisting of a DMF film and a fresh gas phase) to the complete evaporation state is shown in Fig. S3.† A critical gas thickness is a prerequisite (necessary condition) for the complete evaporation of the liquid DMF film. With this critical gas thickness, the liquid DMF film completely evaporates to its gas phase in air mixing with other gases until the partial pressure of DMF gas reaches the saturated vapor pressure at the current temperature in the gas mixture. Actually, only if the gas thickness is equal to or larger than this critical thickness, the liquid phase can completely evaporate. To obtain the critical thickness of the gas mixture at which all solvents have completely evaporated, some calculations were conducted as follows. Based on mass conservation of DMF between the starting liquid state and the final gaseous state, eqn (1) can be introduced:

$$A\delta\rho_l w\% = \frac{AHP^*}{RT} M \tag{1}$$

then, H can be expressed as in eqn (2):

$$H = \frac{\rho_l w\% RT}{P^* M} \delta \tag{2}$$

where A is the solution film area, δ is the solution film thickness, ρ_l is the density of the precursor solution, $w\%$ is the mass fraction of the DMF solvent in solution, H is the gas mixture thickness, P^* is the DMF saturated vapor pressure at the current temperature, R is the gas constant, T is the current temperature, and M is the molar mass of DMF.

To achieve effective and complete solvent evaporation, a sufficient condition should also be satisfied. Evaporation is a process that involves two consecutive steps. The first step entails the evaporation of gas molecules from the solution surface, while the second step involves their transportation far away from the solution surface by diffusion. It can be first analyzed from a microscopic point of view, according to which gas molecules evaporate from the liquid phase. Notably, evaporation is a ubiquitous physical phenomenon involving mass transfer from a liquid phase to a gas phase. Classical evaporation theory gives eqn (3) based on the hypothesis that the gas satisfies the equation of state of an ideal gas and that evaporation and condensation are independent at the gas–liquid interface:[36,37]

$$j = j_+ - j_- = \left(\frac{M}{2\pi R}\right)^{\frac{1}{2}} \left(\frac{P_l}{\sqrt{T_l}} - \frac{P_g}{\sqrt{T_g}}\right) \tag{3}$$

where j is the net mass flow rate, j_+/j_- is the evaporation/condensation mass flow rate, M is the molar mass, P_l is the

saturated vapor pressure at the current temperature, T_l is the liquid temperature, P_g is the partial pressure of the evaporated gas phase, and T_g is the gas temperature. Apparently, j depends on the difference between P_l and P_g, since T_l is generally equal to T_g. Therefore, reducing P_g provides an effective way to increase the net evaporation mass flow rate from a microscopic point of view.

From a macroscopic point of view, evaporated molecules diffuse to far distance where the solvent partial pressure approaches zero. Diffusion depends on the concentration gradient d (eqn (4)):

$$d = \frac{\partial C}{\partial h} \approx \frac{\Delta P}{h} \tag{4}$$

where C is the solvent gas concentration, h is the distance to the liquid surface, and ΔP is the difference of partial pressures at the liquid surface and bulk environment. It is known that evaporated solvent molecules can diffuse quickly at a large concentration gradient. In brief, a fast evaporation can be successfully conducted by significantly reducing P_g and decreasing h.

Comparing different drying methods may help understand more deeply the evaporation process in thin solution films. Natural drying involves the drying of the solution film in its current environment (Fig. 3a). In this case, the net evaporation is very low because most of the gas molecules at the interface return to the liquid phase upon molecular collision. Obviously, in natural drying, the concentration gradient d is extremely small (Fig. 3e), owing to the large h value, and therefore, diffusivity is extremely low. Owing to the slow evaporation, small areas reaching supersaturation—which is necessary for nucleation—are formed on the solution film. Subsequently, the solute nucleates on those areas.[38,39] Additionally, the low evaporation rate facilitates the migration of residual solute and formation of overgrown crystals.[33] Finally, those nuclei grow into a light gray film with large roughness, visible to the naked eye (Fig. 3i). Fig. 3m shows a SEM image and schematic diagram of primal nucleation and growth. The film presented a disorganized branch-like morphology with long strip-like grains up to hundreds of micrometers in size, consistent with the results widely reported in the literature.[40]

Compared with natural drying, appropriate heating can accelerate solvent evaporation (Fig. 3b), as already reported.[10] Heating promotes molecule diffusion, which results from a larger concentration gradient than that observed in natural drying because of the enlarged ΔP value (Fig. 3f). Therefore, more nuclei form on the substrate in a shorter time, growing into thick dendritic grains with sizes tens of micrometers larger (Fig. 3n) than those of the grains observed after natural drying. Correspondingly, the photograph in Fig. 3j displays a deeper gray color and a relatively smoother surface than the sample obtained by natural drying.

Intuitively, blowing air on the surface of a solution film favors the evaporation. The air flow can remove the gas molecules from the solution film surface, reducing the gas solvent partial pressure, P_g, thereby improving the net evaporation mass. Air-assisted evaporation conducted from a large distance
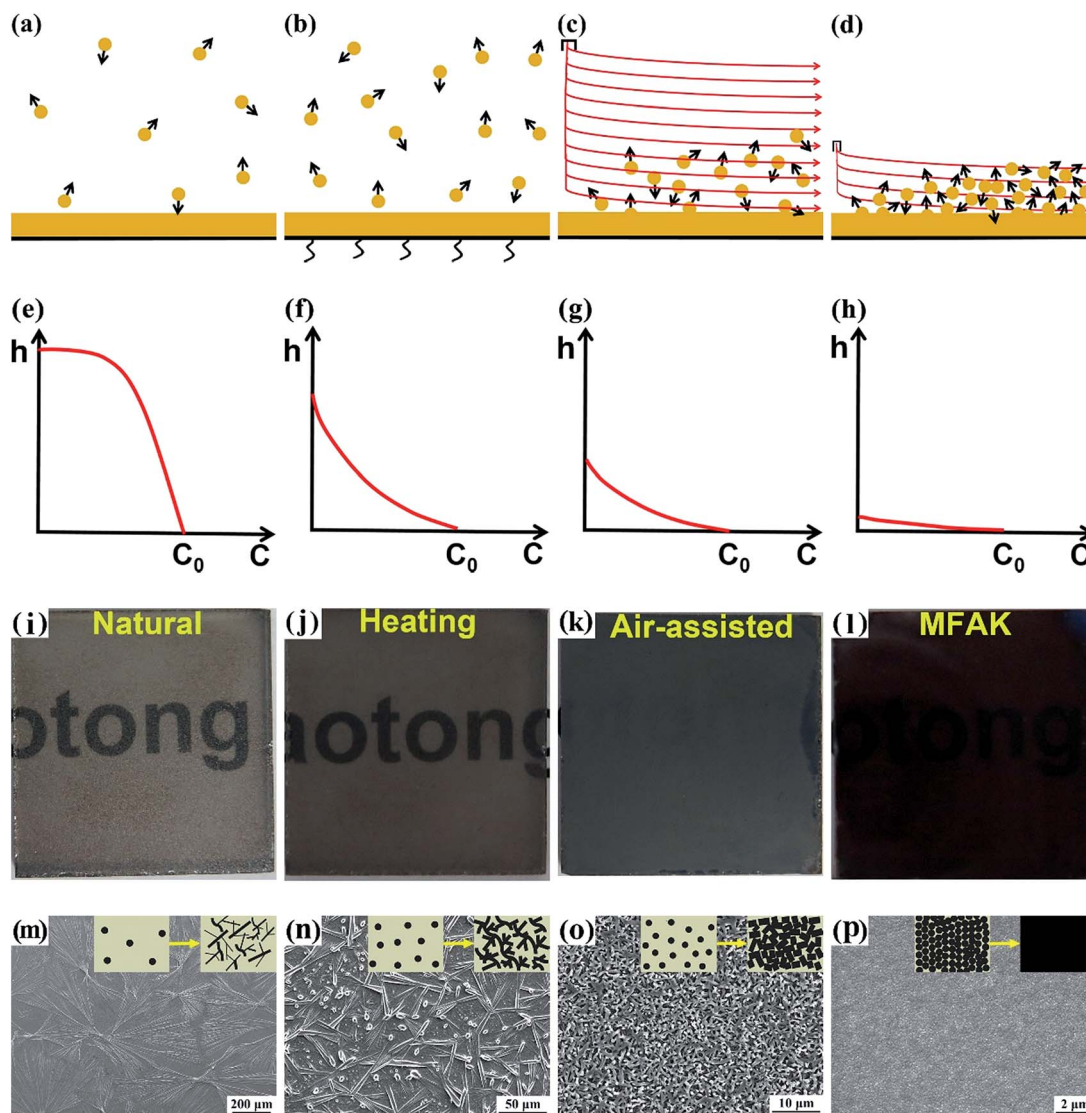
Fig. 3 Liquid *N,N*-dimethylformamide film evaporation under different drying conditions. (a–d) Schematic diagram showing molecule evaporation at the gas–liquid interface for natural, heat, air-assisted, and MAK drying, respectively. (e–h) Concentration gradients with molecule diffusion for natural, heat, air-assisted, and MAK drying, respectively. (i–l) Photographs of natural, heat, air-assisted and MAK dried films, respectively. (m–p) Scanning electron microscopy images and (insets) schematic diagrams of nucleation of natural, heat, air-assisted, and MAK dried liquid perovskite films, respectively.

from the liquid surface (Fig. 3c) removes some gas molecules and reduces P_g, while d increases owing to the reduction in h (Fig. 3h). Compared with the heat-dried film, some improvements were achieved, the film presented a dark gray color (Fig. 3k), and the dendritic grain size decreased by several micrometers (Fig. 3o). However, many pin holes, which are detrimental for the device performance, still existed in the film.[8]

Remarkably, the MAK method provides a qualitative improvement in solvent evaporation, allowing the fabrication of extremely compact films. Due to the MAK blowing in close proximity of the surface, the vast majority of the molecules are effectively removed (Fig. 3d), resulting in a diffusion concentration gradient considerably higher than those observed for all the above mentioned methods (Fig. 3h). The MAK method allows a significant concentration gradient for diffusion of the

evaporated solvent molecules. Consequently, the solvent evaporates instantaneously and uniform nuclei are formed on the substrate. Then, the nuclei grow competitively into closely arranged grains with sizes of hundreds of nanometers (Fig. 3p). The MAK-dried film obviously presented different features from the others, and exhibited a mirror-like black brown morphology (Fig. 3l). In brief, the flexible MAK method can tremendously facilitate the solution evaporation and molecule diffusion, allowing an adequate air blow from a short distance to dry the solution film. Besides, the solution film size is unlimited. Thus, industrialized manufacturing at the meter scale can be easily realized by concurrently adjusting the length of the air knife to the meter scale.

To explore the effects of film morphology on device performance, the four different kinds of films described above were

used to prepare distinct devices, whose efficiencies showed significant differences (Fig. S4†). The device containing the naturally dried film achieved 0.89% efficiency, whereas a slightly higher efficiency (1.48%) was obtained for the device employing the heat-dried film. The device with the film dried by using an air-assisted procedure reached 8.72% efficiency, whereas an extremely high efficiency of 17.26% was achieved by the device using the MAK-dried film. The device efficiency improved greatly with film coverage rate increasing. The device energy conversion efficiency can be attributed to incomplete surface coverage resulting from cell shunting and poor light absorption.[8,40]

Crystallization and optical properties of the perovskite film

The MAK-dried perovskite film was examined by X-ray diffraction (XRD) to investigate its crystallization (Fig. 4a). Clear diffraction peaks at 14.08°, 28.40°, and 31.83° could be assigned to the (110), (220), and (310) planes, respectively, revealing the presence of the $CH_3NH_3PbI_3$ tetragonal phase (space group $I4/mcm$, $a = b = 8.8743$ Å, and $c = 12.6708$ Å). No diffraction peaks of PbI_2 or CH_3NH_3I were found in the pattern of the $CH_3NH_3PbI_3$ crystals, indicating that the entire compound reacted completely during the MAK drying process.

To evaluate the optical properties of the perovskite film, the ultraviolet-visible absorption and photoluminescence (PL) spectra (Fig. 4b) were analyzed. The spectra exhibited very high absorption in the visible range of 380–760 nm, showing remarkable intensity at ~500 nm, which is consistent with the results reported in the literature.[41,42] The static PL spectrum, excited at the wavelength of 560 nm, showed strong intensity at the wavelength of ~780 nm, in good agreement with previous results.[43] The excellent optical properties may be probably ascribed to the low defect density in the bulk of the perovskite film.

Dependence of perovskite film quality on processing parameters

To investigate the quantitative relationship between the perovskite film microstructure and the processing parameters, perovskite films dried by using the MAK method were prepared by controlling two main processing parameters, *i.e.*, air flow and distance between the air knife and the liquid surface. After

being dried at 300 L min⁻¹ and 1 mm (air flow rate and distance between the air knife and the solution film surface, respectively), at the current temperature, the dried perovskite film appeared black-brown transparent with a mirror-like surface. When the air flow rate was lower than 300 L min⁻¹ or the distance higher than 1 mm, the dried perovskite film became blurry and opaque, as shown by the photographs in Fig. S5.† To investigate quantitatively their microscopic morphology and surface roughness, the MAK-dried perovskite films were measured by SEM and high-resolution AFM (Fig. 5). The measurement was performed on a randomly chosen large and uniform perovskite film. The AFM scanning area was 10×10 μm².

First, the influence of the air flow on film morphology was analyzed. Upon increasing the air flow at the distance of 1 mm, the perovskite films acquired a more compact and smooth morphology. Fig. 5a shows the morphology of the film dried at 150 L min⁻¹; large rod-like grains and some pin holes were visible, while the cross-sectional image showed the bare substrate, revealing incomplete perovskite coverage. The film root-mean-square (RMS) roughness was 21.28 nm, as shown by the AFM morphology (Fig. 5b). Fig. 5c shows the three-dimensional morphology and roughness fluctuation profile along the line in Fig. 5b. The large fluctuation indicated that the surface of the film was seriously coarse. By increasing the air flow to 225 L min⁻¹, the film exhibited smaller dendrite grains and a reduced number of pin holes, while the cross-sectional image showed an irregular cross-section (Fig. 5d). The film had a RMS of 15.0 nm, showing a smaller fluctuation than the film dried at 150 L min⁻¹ (Fig. 5e and f). Interestingly, when the air flow increased to 300 L min⁻¹, the perovskite film showed an extraordinarily compact and pin-hole free morphology (Fig. 5g). The grains, shown in the cross-sectional image, appeared as columnar crystals having a regular and close arrangement. The extremely smooth film RMS was only 4.98 nm (Fig. 5h). The slight fluctuation on the film surface was just in the range of 20 nm, significantly lower than the thickness of the compact film, ~300 nm (Fig. 5i). The examination was also conducted randomly over a large area of 20×20 μm², finding an RMS of 5.03 nm (Fig. S6†). Thus, air flow of sufficient rate can efficiently remove DMF molecules, significantly reducing the P_g value, accelerating the evaporation, and thus producing a full-coverage perovskite film.

Subsequently, we further examined the influence of the distance between the air knife and the liquid surface on the film morphology. The perovskite film was dried at the distance of 5 mm, using an air flow rate of 300 L min⁻¹. The analyses of both the surface and cross-sectional morphologies showed a film with small rod-like grains along with the bare substrate (Fig. 5j). The film had an RMS of 39.6 nm and a fluctuation (Fig. 5k and l) significantly larger than the film dried at the distance of 1 mm by using the same air flow rate. The smaller concentration gradient over a long distance cannot remove more molecules because of the difficult diffusion. The distance of 5 mm between the MAK and the solution film surface resulted in an air flow speed slower than that observed in the case of the distance of 1 mm at the same air flow rate. Therefore,
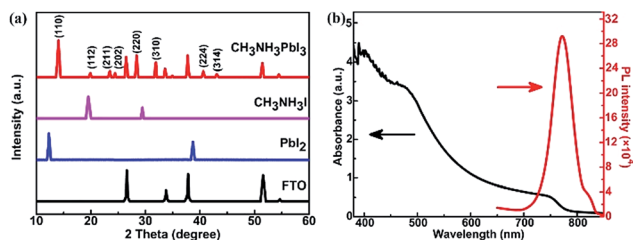

Fig. 4 (a) X-ray diffraction patterns of the perovskite film dried by the multi-flow air knife method, CH_3NH_3I particles, PbI_2 particles, and the fluorine-doped tin oxide substrate. (b) Ultraviolet-visible absorption and photoluminescence spectra of the perovskite film.
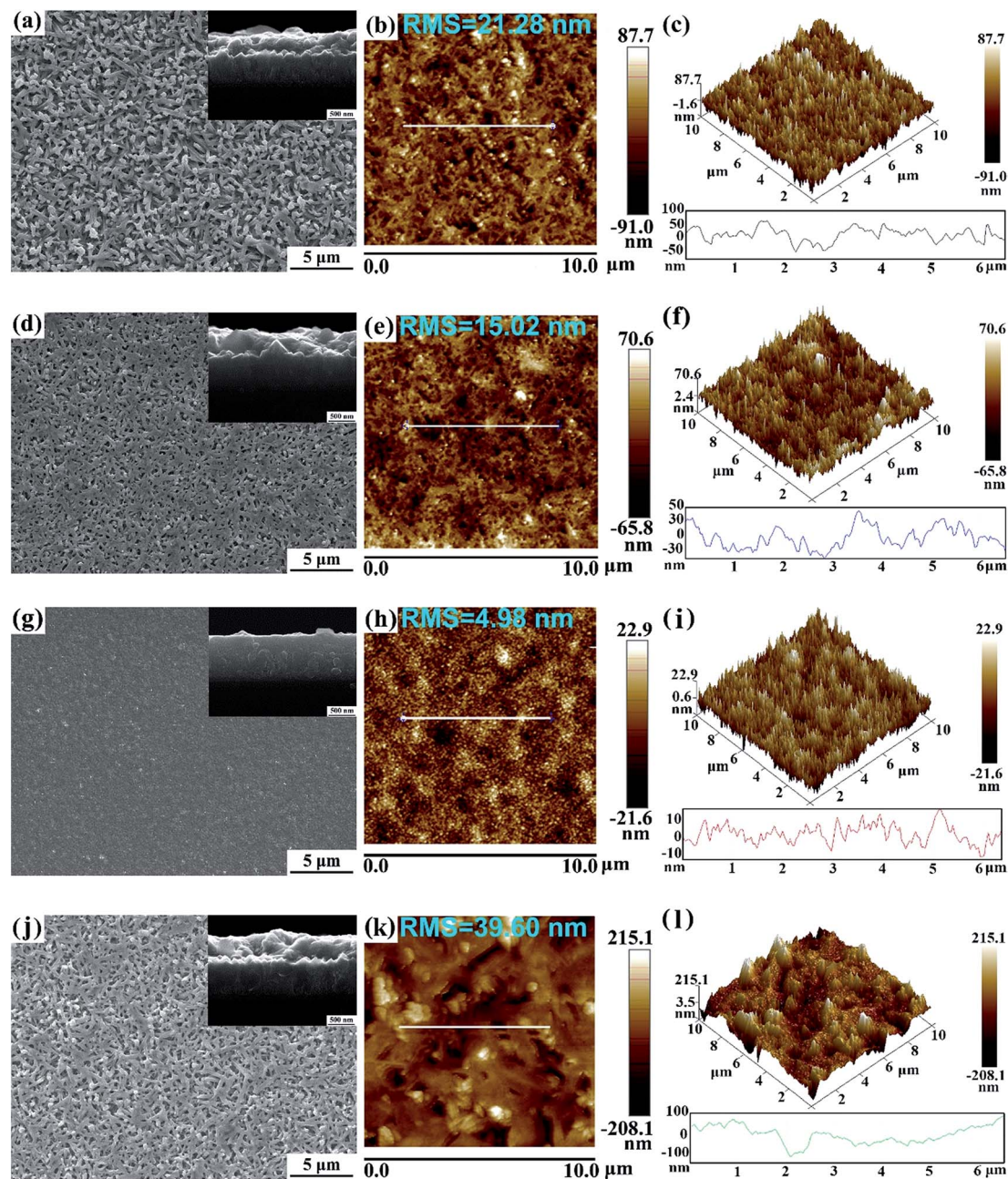
Fig. 5 Scanning electron microscopy (SEM) and atomic force microscopy images of perovskite films dried by the MAK method under different conditions. Perovskite films dried at: (a–c) 150 L min^{-1} and 1 mm; (d–f) 225 L min^{-1} and 1 mm; (g–i) 300 L min^{-1} and 1 mm; (j–l) 300 L min^{-1} and 5 mm; the insets in (a), (d), (g), and (j) show the cross-sectional SEM images of the perovskite films.

the perovskite film could not be properly dried at a large distance. A large concentration gradient is crucial to achieve a quick evaporation. The MAK method is highly efficient in drying perovskite films when using an appropriate air flow in close proximity.

Besides, more detailed experiments confirmed the above conclusions. The comparative results are shown in Fig. S7.† The perovskite film showed small pin holes and an isometric crystal morphology when dried at 150 L min^{-1} and 0.5 mm, as shown in Fig. S7a.† When the distance increased to 1 mm, the perovskite film exhibited pin holes and dendritic structures of larger

sizes, as shown in Fig. S7b.† Similarly, a change was also observed when the film was dried at 225 L min^{-1}, as shown in Fig. S7c and d.† This film presented smaller pin holes and shorter dendritic structures than that dried at 150 L min^{-1} at the same distance. Fig. S7e–i† show the film dried at 300 L min^{-1} with distances ranging from 1 to 5 mm, respectively. The perovskite film dried at a close distance exhibited a compact pin-hole free morphology with uniform isometric crystals. Upon increasing the distance, some pin holes appeared, and their size and number increased dramatically. Crystalline grains also transformed from uniform compact

1554 | J. Mater. Chem. A, 2017, 5, 1548–1557

This journal is © The Royal Society of Chemistry 2017

isometric to large dendritic crystals. The larger the distance between the MAK and the liquid surface, the larger the dendritic structure. Finally, the perovskite film presented a discontinuous morphology. An adequate air flow can remove more solvent molecules at a short distance, producing a larger concentration gradient. Therefore, a compact pin-hole free perovskite film can be obtained by using suitable parameters, for example an air flow rate of 300 L min^{-1} and a distance of 1 mm.

Photovoltaic performance of perovskite solar cells

To investigate the effects of the MAK-dried perovskite film morphology on the device performance, planar heterojunction perovskite-based solar cells were fabricated with active areas of 1 and 0.1 cm^2. Each small piece of perovskite-coated substrate was cut from a larger perovskite film prepared by using the MAK method. Upon analysis of over 40 devices with an active area of 1 cm^2, the highest efficiency was 11.70%, while the average efficiency was 10.20 ± 0.81%. Even higher efficiency was achieved for small-area devices, upon measuring 40 devices with an active area of 0.1 cm^2, the highest efficiency of 17.71% and average efficiency of 14.42 ± 1.34% were found. Clearly, this demonstrated the promising potential of this technology for the production of highly efficient perovskite solar cells.

Fig. 6a shows the cross-sectional SEM image of the devices. The structure consisted of a fluorine-doped tin oxide (FTO)

coated glass, TiO$_2$ compact layer, MAK-dried CH$_3$NH$_3$PbI$_3$ perovskite absorber, spiro-OMeTAD hole transport layer, and thermally evaporated Au contact (FTO/TiO$_2$/CH$_3$NH$_3$PbI$_3$/spiro-OMeTAD/Au). Fig. 6b shows the corresponding energy levels for every layer. All layers were fabricated and characterized in an ambient atmosphere except for the thermally evaporated Au cathode. The best cells with efficiencies of 11.70% and 17.71% were fabricated with perovskite films dried at 300 L min^{-1} and 1 mm. Fig. 6c shows the I–V curves of the best device (area of 1.0 cm^2). The V_{oc} was 1.09 V (which is comparable to the V_{oc} values of the top-performing large-area devices based on the same materials),[17,18,30,44] J_{sc} was 17.62 mA cm^{-2}, FF was 0.612, and PCE was 11.70%. Fig. 6d shows the corresponding incident photon-to-current conversion efficiency (IPCE) spectrum and the integrated current density as a function of the wavelength. The integrated J_{sc}, calculated from the IPCE spectrum, was 15.46 mA cm^{-2}, which was roughly comparable with that obtained from the I–V curves. Furthermore, perovskite solar cells with an active area of 0.1 cm^2 reached the highest efficiency of 17.71% (the I–V curves are shown in Fig. 6e), while J_{sc} was 23.50 mA cm^{-2}, V_{oc} was 1.09 V, and FF was 0.69. To investigate the carrier transport and recombination behaviors in this device, electrochemical impedance spectroscopy (EIS) analysis was conducted. Fig. 6f shows the Nyquist plots over the frequency range from 4 MHz to 100 mHz at the forward bias range of 0.0–1.0 V and illumination of 37 W m^2. Subsequently, the Nyquist plots were fitted using the RC equivalent circuit diagram,[45,46] as shown in the inset of Fig. 6f. Notably, two distinct arcs could be observed in two distinct frequency regions in each EIS spectrum. The first arc in the high-frequency region is usually attributed to the carrier transport process at the interface in the device, while the second arc at low frequency is usually related to the charge recombination within the perovskite film and the interface of the charge transport layer.[47,48] By increasing the forward bias, the two arcs became larger, which indicated increases in carrier transport and recombination resistances.

Furthermore, a large active area device of 1.47 cm^2 with the same size mask was measured. The high efficiency is up to 11.12%, as shown in Fig. S8.† And the MAK method showed good reproducibility due to the well-controlled film quality. The average efficiency reached stably a value of 10.20 ± 0.81% for 40 solar cells with an active area of 1 cm^2 and 14.42 ± 1.34% for 40 solar cells with an active area of 0.1 cm^2. The device parameter distributions are shown in Fig. S9.† All those cells showed high V_{oc}, and the highest V_{oc} value, obtained for the cell with area of 1 cm^2, was 1.10 V, which is the highest value obtained for devices with an area of 1 cm^2 fabricated with the same materials. The average V_{oc} for 40 solar cells with an area of 1 cm^2 was 1.05 ± 0.03 V, which indicated the formation of a full-coverage compact perovskite film upon drying by using the MAK method over a large active area. Similarly, the highest V_{oc} and average V_{oc} values for 40 solar cells with an area of 0.1 cm^2 were 1.09 V and 1.05 ± 0.02 V, respectively. Statistically, 97.5% of the cells exhibited a V_{oc} higher than 1 V. Thus, the MAK method is extremely valuable to prepare perovskite films in a scalable size.
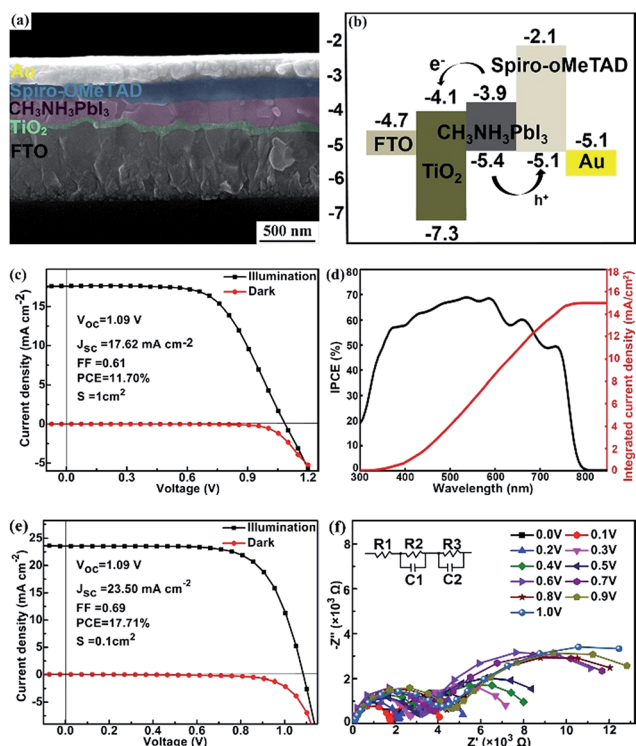

Fig. 6 (a) Cross-sectional scanning electron microscopy image of the perovskite solar cell. (b) Energy level alignment for every device layer. (c) Current−voltage (I–V) curve for the best device with an active area of 1 cm^2 from short-circuit to forward bias (SC−FB) and (d) the corresponding incident photon to current conversion efficiency spectrum. (e) I–V curve for the best device with an active area of 0.1 cm^2 and (f) the corresponding electrochemical impedance spectrum.

This journal is © The Royal Society of Chemistry 2017

J. Mater. Chem. A, 2017, 5, 1548–1557 | **1555**

In addition, some comparative experiments were also conducted with perovskite films dried by using different air flow rates and distances. The device parameters are reported in Tables S1 and S2.† Clearly, devices using compact perovskite films dried at 300 L min^{-1} and 1 mm presented excellent electrical performances. This can be attributed to the fact that the defects in the perovskite film reduce the light absorption ability and increase the recombination at the interface between the electron transport layer and the hole transport layer.[8] In addition, pin holes, or even the bare substrate without perovskite coverage, would inevitably reduce current shunting in the carrier transport, degrading the device performance.[40]

Conclusions

In summary, we first demonstrated the fabrication of highly efficient perovskite solar cells based on perovskite films dried by using the novel MAK technology at room temperature in ambient air. We reported a record efficiency of 11.70% for large-area perovskite solar cells (active area of 1 cm^2) at room temperature in ambient air. By adopting the MAK method, we produced uniform, pin-hole free, large crystal grain size and rough-border-free perovskite films with a RMS of 4.98 nm. This method is highly efficient for drying solution films without any limitation on solvent and film size, and therefore can be easily applied to large-area meter-scale industrial mass production. Planar perovskite solar cells with an active area of 1 cm^2 containing the fabricated films exhibited the highest efficiency of 11.70%. The devices also showed excellent reproducibility due to the high-quality films, reaching the average efficiency of 10.20% ± 0.81% over 40 solar cells. In addition, for the device with an active area of 0.1 cm^2, the highest efficiency of 17.71% was obtained, which further suggested the promising potential of the MAK technology. We believe that the novel MAK method will tremendously promote the low-cost mass production of highly efficient perovskite solar cells, also providing a broad view for fabricating high-quality perovskite films by adopting alternative solution processes.

Acknowledgements

Notes and references

1 A. Kojima, K. Teshima, Y. Shirai and T. Miyasaka, *J. Am. Chem. Soc.*, 2009, **131**, 6050–6051.

2 W. S. Yang, J. H. Noh, N. J. Jeon, Y. C. Kim, S. Ryu, J. Seo and S. I. Seok, *Science*, 2015, **348**, 1234–1237.

3 D. Q. Bi, W. Tress, M. I. Dar, P. Gao, J. S. Luo, C. Renevier, K. Schenk, A. Abate, F. Giordano, J. P. C. Baena, J. D. Decoppet, S. M. Zakeeruddin, M. K. Nazeeruddin, M. Gratzel and A. Hagfeldt, *Sci. Adv.*, 2016, **2**, e1501170.

4 M. Saliba, T. Matsui, J. Y. Seo, K. Domanski, J. P. Correa-Baena, M. K. Nazeeruddin, S. M. Zakeeruddin, W. Tress, A. Abate, A. Hagfeldt and M. Gratzel, *Energy Environ. Sci.*, 2016, **9**, 1989–1997.

5 Q. Dong, Y. Fang, Y. Shao, P. Mulligan, J. Qiu, L. Cao and J. Huang, *Science*, 2015, **347**, 967–970.

6 S. D. Stranks, G. E. Eperon, G. Grancini, C. Menelaou, M. J. Alcocer, T. Leijtens, L. M. Herz, A. Petrozza and H. J. Snaith, *Science*, 2013, **342**, 341–344.

7 D. Shi, V. Adinolfi, R. Comin, M. J. Yuan, E. Alarousu, A. Buin, Y. Chen, S. Hoogland, A. Rothenberger, K. Katsiev, Y. Losovyj, X. Zhang, P. A. Dowben, O. F. Mohammed, E. H. Sargent and O. M. Bakr, *Science*, 2015, **347**, 519–522.

8 G. E. Eperon, V. M. Burlakov, P. Docampo, A. Goriely and H. J. Snaith, *Adv. Funct. Mater.*, 2014, **24**, 151–157.

9 F. X. Xie, D. Zhang, H. Su, X. Ren, K. S. Wong, M. Grätzel and W. C. Choy, *ACS Nano*, 2015, **9**, 639–646.

10 F. Z. Huang, Y. Dkhissi, W. C. Huang, M. D. Xiao, I. Benesperi, S. Rubanov, Y. Zhu, X. F. Lin, L. C. Jiang, Y. C. Zhou, A. Gray-Weale, J. Etheridge, C. R. McNeill, R. A. Caruso, U. Bach, L. Spiccia and Y. B. Cheng, *Nano Energy*, 2014, **10**, 10–18.

11 F. Wang, H. Yu, H. Xu and N. Zhao, *Adv. Funct. Mater.*, 2015, **25**, 1120–1126.

12 N. J. Jeon, J. H. Noh, Y. C. Kim, W. S. Yang, S. Ryu and S. I. Seok, *Nat. Mater.*, 2014, **13**, 897–903.

13 Q. Chen, H. Zhou, Z. Hong, S. Luo, H. S. Duan, H. H. Wang, Y. Liu, G. Li and Y. Yang, *J. Am. Chem. Soc.*, 2014, **136**, 622–625.

14 W. Y. Nie, H. H. Tsai, R. Asadpour, J. C. Blancon, A. J. Neukirch, G. Gupta, J. J. Crochet, M. Chhowalla, S. Tretiak, M. A. Alam, H. L. Wang and A. D. Mohite, *Science*, 2015, **347**, 522–525.

15 J. H. Park, J. Seo, S. Park, S. S. Shin, Y. C. Kim, N. J. Jeon, H. W. Shin, T. K. Ahn, J. H. Noh, S. C. Yoon, C. S. Hwang and S. I. Seok, *Adv. Mater.*, 2015, **27**, 4013–4019.

16 N. J. Jeon, J. H. Noh, W. S. Yang, Y. C. Kim, S. Ryu, J. Seo and S. I. Seok, *Nature*, 2015, **517**, 476–480.

17 F. Ye, H. Chen, F. Xie, W. Tang, M. Yin, J. He, E. Bi, Y. Wang, X. Yang and L. Han, *Energy Environ. Sci.*, 2016, **9**, 2295–2301.

18 W. Chen, Y. Wu, Y. Yue, J. Liu, W. Zhang, X. Yang, H. Chen, E. Bi, I. Ashraful and M. Grätzel, *Science*, 2015, **350**, 944–948.

19 P. P. Boix, K. Nonomura, N. Mathews and S. G. Mhaisalkar, *Mater. Today*, 2014, **17**, 16–23.

20 S. T. Williams, A. Rajagopal, C. C. Chueh and A. K. Y. Jen, *J. Phys. Chem. Lett.*, 2016, **7**, 811–819.

21 A. T. Barrows, A. J. Pearson, C. K. Kwak, A. D. F. Dunbar, A. R. Buckley and D. G. Lidzey, *Energy Environ. Sci.*, 2014, **7**, 2944–2950.

22 J. Y. Jeng, Y. F. Chiang, M. H. Lee, S. R. Peng, T. F. Guo, P. Chen and T. C. Wen, *Adv. Mater.*, 2013, **25**, 3727–3732.

23 Z. B. Yang, C. C. Chueh, F. Zuo, J. H. Kim, P. W. Liang and A. K. Y. Jen, *Adv. Energy Mater.*, 2015, **5**, 1500328.

24 Y. Deng, E. Peng, Y. Shao, Z. Xiao, Q. Dong and J. Huang, *Energy Environ. Sci.*, 2015, **8**, 1544–1550.

25 K. Li, H. Y. Zhen, L. Y. Niu, X. Fang, Y. K. Zhang, R. S. Guo, Y. Yu, F. Yan, H. F. Li and Z. J. Zheng, *Adv. Mater.*, 2014, **26**, 7271–7278.

26 Z. H. Wei, H. N. Chen, K. Y. Yan and S. H. Yang, *Angew. Chem., Int. Ed.*, 2014, **53**, 13239–13243.

27 K. Hwang, Y. S. Jung, Y. J. Heo, F. H. Scholes, S. E. Watkins, J. Subbiah, D. J. Jones, D. Y. Kim and D. Vak, *Adv. Mater.*, 2015, **27**, 1241–1247.

28 L.-L. Gao, L.-S. Liang, X.-X. Song, B. Ding, G.-J. Yang, B. Fan, C.-X. Li and C.-J. Li, *J. Mater. Chem. A*, 2016, **4**, 3704–3710.

29 Y. Li, X. L. He, B. Ding, L. L. Gao, G. J. Yang, C. X. Li and C. J. Li, *J. Power Sources*, 2016, **320**, 204–211.

30 B. Ding, L. Gao, L. Liang, Q. Chu, X. Song, Y. Li, G. Yang, B. Fan, M. Wang, C. Li and C. Li, *ACS Appl. Mater. Interfaces*, 2016, **8**, 20067–20073.

31 X. Li, D. Q. Bi, C. Y. Yi, J. D. Decoppet, J. S. Luo, S. M. Zakeeruddin, A. Hagfeldt and M. Gratzel, *Science*, 2016, **353**, 58–62.

32 N. Li, H. Dong, H. Dong, J. Li, W. Li, G. Niu, X. Guo, Z. Wu and L. Wang, *J. Mater. Chem. A*, 2014, **2**, 14973–14978.

33 M. Zhang, H. Yu, J. H. Yun, M. Q. Lyu, Q. Wang and L. Z. Wang, *Chem. Commun.*, 2015, **51**, 10038–10041.

34 V. O. Eze, B. Lei and T. Mori, *Jpn. J. Appl. Phys.*, 2016, **55**, 02BF08.

35 S. Razza, F. Di Giacomo, F. Matteocci, L. Cina, A. L. Palma, S. Casaluci, P. Cameron, A. D'epifanio, S. Licoccia and A. Reale, *J. Power Sources*, 2015, **277**, 286–291.

36 T. Tsuruta, H. Tanaka and T. Masuoka, *Int. J. Heat Mass Transfer*, 1999, **42**, 4107–4116.

37 I. Eames, N. Marr and H. Sabir, *Int. J. Heat Mass Transfer*, 1997, **40**, 2963–2973.

38 J. H. Heo, D. H. Song and S. H. Im, *Adv. Mater.*, 2014, **26**, 8179–8183.

39 T. Baikie, Y. Fang, J. M. Kadro, M. Schreyer, F. Wei, S. G. Mhaisalkar, M. Graetzel and T. J. White, *J. Mater. Chem. A*, 2013, **1**, 5628–5641.

40 M. D. Xiao, F. Z. Huang, W. C. Huang, Y. Dkhissi, Y. Zhu, J. Etheridge, A. Gray-Weale, U. Bach, Y. B. Cheng and L. Spiccia, *Angew. Chem., Int. Ed.*, 2014, **53**, 9898–9903.

41 S. A. Kulkarni, T. Baikie, P. P. Boix, N. Yantara, N. Mathews and S. Mhaisalkar, *J. Mater. Chem. A*, 2014, **2**, 9221–9225.

42 O. Malinkiewicz, . Yella, Y. H. Lee, G. M. Espallargas, M. Graetzel, M. K. Nazeeruddin and H. J. Bolink, *Nat. Photonics*, 2014, **8**, 128–132.

43 B. Wang, K. Y. Wong, S. Yang and T. Chen, *J. Mater. Chem. A*, 2016, **4**, 3806–3812.

44 M. Yang, Y. Zhou, Y. Zeng, C. S. Jiang, N. P. Padture and K. Zhu, *Adv. Mater.*, 2015, **27**, 6363–6370.

45 D. Li, J. Cui, H. Li, D. K. Huang, M. K. Wang and Y. Shen, *Sol. Energy*, 2016, **131**, 176–182.

46 M. J. Yang, R. Guo, K. Kadel, Y. Y. Liu, K. O'Shea, R. Bone, X. W. Wang, J. He and W. Z. Li, *J. Mater. Chem. A*, 2014, **2**, 19616–19622.

47 J. W. Jung, C. C. Chueh and A. K. Y. Jen, *Adv. Mater.*, 2015, **27**, 7874–7880.

48 J. A. Christians, R. C. Fung and P. V. Kamat, *J. Am. Chem. Soc.*, 2013, **136**, 758–764.